

# On-sky Performance of the CLASS Q-band Telescope

John W. Appel<sup>1</sup>, Zhilei Xu (徐智磊)<sup>1,2</sup>, Ivan L. Padilla<sup>1</sup>, Kathleen Harrington<sup>1,3</sup>, Bastián Pradenas Marquez<sup>4</sup>, Aamir Ali<sup>1,5</sup>, Charles L. Bennett , Michael K. Brewer, Ricardo Bustos , Manwei Chan, David T. Chuss, Joseph Cleary, Jullianna Couto<sup>1</sup>, Sumit Dahal<sup>1</sup>, Kevin Denis<sup>8</sup>, Rolando Dünner<sup>9</sup>, Joseph R. Eimer<sup>1</sup>, Thomas Essinger-Hileman<sup>8</sup>, Pedro Fluxa <sup>9</sup>, Dominik Gothe <sup>1</sup>, Gene C. Hilton <sup>10</sup>, Johannes Hubmayr <sup>10</sup>, Jeffrey Iuliano <sup>1</sup>, John Karakla <sup>1</sup>, Tobias A. Marriage <sup>1</sup>, Nathan J. Miller <sup>1,8</sup>, Carolina Núñez <sup>1</sup>, Lucas Parker <sup>1,11</sup>, Matthew Petroff <sup>1</sup>, Carl D. Reintsema <sup>10</sup>, Karwan Rostem <sup>8</sup>, Robert W. Stevens<sup>10</sup>, Deniz Augusto Nunes Valle<sup>1</sup>, Bingjie Wang (王冰洁)<sup>1</sup>, Duncan J. Watts<sup>1</sup>, Edward J. Wollack<sup>8</sup>, and Lingzhen Zeng<sup>12</sup> Department of Physics and Astronomy, Johns Hopkins University, 3701 San Martin Drive, Baltimore, MD 21218, USA; jappel3@jhu.edu Department of Physics and Astronomy, University of Pennsylvania, 209 South 33rd Street, Philadelphia, PA 19104, USA

3 Department of Physics, University of Michigan, Ann Arbor, MI, 48109, USA <sup>4</sup> Departamento de Física, FCFM, Universidad de Chile, Blanco Encalada 2008, Santiago, Chile Department of Physics, University Of California, Berkeley, CA 94720, USA <sup>6</sup> Facultad de Ingeniería, Universidad Católica de la Santísima Concepción, Alonso de Ribera 2850, Concepción, Chile Department of Physics, Villanova University, 800 Lancaster Avenue, Villanova, PA 19085, USA Goddard Space Flight Center, 8800 Greenbelt Road, Greenbelt, MD 20771, USA <sup>9</sup> Instituto de Astrofísica and Centro de Astro-Ingeniería, Facultad de Física, Pontificia Universidad Católica de Chile, Av. Vicuña Mackenna 4860, 7820436 Macul, Santiago, Chile <sup>10</sup> Quantum Sensors Group, National Institute of Standards and Technology, 325 Broadway, Boulder, CO 80305, USA

Oquantum Sensors Group, National Institute of Standards and Technology, 325 Broadway, Boulder, CO 80305, USA

11 Space and Remote Sensing, MS D436, Los Alamos National Laboratory, Los Alamos, NM 87544, USA

12 Harvard-Smithsonian Center for Astrophysics: Cambridge, MA, USA

Received 2018 November 17; revised 2019 March 20; accepted 2019 April 3; published 2019 May 10

#### **Abstract**

The Cosmology Large Angular Scale Surveyor (CLASS) is mapping the polarization of the cosmic microwave background (CMB) at large angular scales ( $2 < \ell \lesssim 200$ ) in search of a primordial gravitational wave B-mode signal down to a tensor-to-scalar ratio of  $r \approx 0.01$ . The same data set will provide a near sample-variance-limited measurement of the optical depth to reionization. Between 2016 June and 2018 March, CLASS completed the largest ground-based Q-band CMB survey to date, covering over 31,000 square-degrees (75% of the sky), with an instantaneous array noise-equivalent temperature sensitivity of  $32~\mu K_{cmb} \sqrt{s}$ . We demonstrate that the detector optical loading (1.6 pW) and noise-equivalent power (19 aW  $\sqrt{s}$ ) match the expected noise model dominated by photon bunching noise. We derive a  $13.1 \pm 0.3~K~pW^{-1}$  calibration to antenna temperature based on Moon observations, which translates to an optical efficiency of  $0.48 \pm 0.02$  and a 27 K system noise temperature. Finally, we report a Tau A flux density of  $308 \pm 11~Jy$  at  $38.4 \pm 0.2~GHz$ , consistent with the *Wilkinson Microwave Anisotropy Probe* Tau A time-dependent spectral flux density model.

*Key words:* cosmic background radiation – cosmology: observations – inflation – instrumentation: detectors – ISM: supernova remnants – Moon

## 1. Introduction

Mapping the polarization of the cosmic microwave background (CMB) is essential for understanding the earliest moments of the universe. In addition to constraining inflation (Guth 1981; Sato 1981; Albrecht & Steinhardt 1982; Linde 1982; Starobinsky 1982; Planck Collaboration et al. 2018b) and the standard six-parameter  $\Lambda$ CDM model (Hinshaw et al. 2013; Planck Collaboration et al. 2018a), the polarization of the CMB is a probe for the epoch of reionization and the growth of largescale structure. The  $100 \,\mu\mathrm{K}$  CMB intensity fluctuations are polarized by Thomson scattering at the few percent level (Rees 1968; Kovac et al. 2002). This polarization is decomposed into E-modes, which provide our best constraint on the optical depth to reionization (Hinshaw et al. 2013; Planck Collaboration et al. 2018a), and B-modes, which probe inflationary gravitational radiation (Kamionkowski et al. 1997; Zaldarriaga & Seljak 1997). The B-mode component is at least 10 times fainter than the E-mode component (BICEP2 Collaboration et al. 2018). Both must be separated from polarized Galactic emission (e.g., BICEP2 Collaboration et al. 2016). Averaged over the sky at high galactic latitudes, polarized dust emission is the dominant Galactic component at frequencies above 70 GHz (Planck Collaboration et al. 2015, 2016b; Planck Collaboration Int. L. 2017; Planck Collaboration et al. 2018d), while synchrotron is the strongest polarized emission mechanism at lower frequencies (Bennett et al. 2013; Planck Collaboration et al. 2018c). On small angular scales gravitational lensing of E-modes induces a B-mode signal larger than the current upper limit on primordial inflationary B-modes. Efforts toward characterizing these small angular scale B-modes include Polarbear Collaboration et al. (2014), Louis et al. (2017), and Henning et al. (2018).

The Cosmology Large Angular Scale Surveyor (CLASS) will measure the polarized microwave sky in bands centered at approximately 40 GHz, 90 GHz, 150 GHz, and 220 GHz from an altitude of 5200 m above sea level in the Atacama Desert of northern Chile (Essinger-Hileman et al. 2014; Harrington et al. 2016) inside the Parque Astronómico Atacama (Bustos et al. 2014). The *Q*-band (40 GHz) telescope probes synchrotron emission (Eimer et al. 2012; Appel et al. 2014), whereas the *G*-band (dichroic 150 and 220 GHz) telescope maps dust. Two *W*-band (90 GHz) telescopes provide the necessary sensitivity to the CMB polarized signal (Dahal et al. 2018). The location,

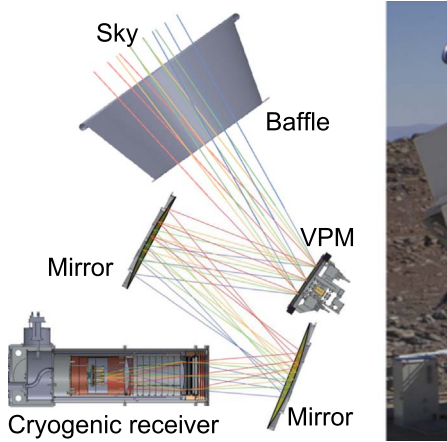




**Figure 1.** Left: diagram of the Q-band instrument including baffle, VPM, mirrors, and cryostat (Eimer et al. 2012; Appel et al. 2014; Essinger-Hileman et al. 2014; Harrington et al. 2016, 2018). For a closer view of the Q-band detector assembly and cryogenic receiver, see Figure 1 in Appel et al. (2014), Rostem et al. (2014b), and Figure 8 in Harrington et al. (2016). Right: photograph of the Q-band telescope configuration during the 2016 June to 2018 March observing period. The telescope is enclosed in a metal structure that protects the instruments and prevents pickup from terrestrial sources.

design, and survey strategy of the CLASS telescopes are defined to reconstruct the microwave polarization at large angular scales (multipoles  $2 < \ell \lesssim 200$ ) over 75% of the sky. To achieve this goal, CLASS employs a variable-delay polarization modulator (VPM) as its first optical element to increase stability and mitigate instrumental polarization (Chuss et al. 2012a; Miller et al. 2016). The benefits of implementing a fast (~10 Hz) polarization modulator as your first optical element has been demonstrated from the ground by the Atacama B-mode Search experiment (Kusaka et al. 2014, 2018). Telescope boresight rotation and a comoving ground shield mitigate contamination by terrestrial polarization sources. The CLASS survey is forecast to constrain the optical depth to reionization  $\tau$  to near the cosmic variance limit and the inflationary tensor-to-scalar ratio to  $r \approx 0.01$  (Watts et al. 2015, 2018). The optical depth is the least constrained  $\Lambda$ CDM parameter, and new measurements at  $\ell < 12$  are important for realizing the full potential of cosmological probes of neutrino masses (Allison et al. 2015; Watts et al. 2018).

This is the first paper describing the on-sky performance of CLASS. This analysis is based on observations with the CLASS Q-band telescope between 2016 June and 2018 March (see Figure 1). In this paper we discuss the calibration and performance of the Q-band telescope for intensity measurements, leaving discussions of polarized performance to future papers. In Section 2, we present median detector parameters extracted from I-V measurements and array sensitivity estimates based on the power spectral density (PSD) of the time-ordered data (TOD). In Section 3, observations of the Moon are used to constrain the average detector beam, the relative gain between detectors, the telescope optical efficiency, and the calibration factor to convert power measured at the detectors to antenna temperature. Using this Moon-based antenna temperature calibration, we present a new measurement of Tau A flux density at Q band in Section 4. Finally, Section 5 summarizes the CLASS Q-band detector array performance during its first observing campaign.

## 2. On-sky Detector Characteristics

The Q-band array consists of 36 feedhorn-coupled, dualpolarization detectors. Each polarimeter has two transition edge sensor (TES) bolometers, one for measuring the optical power in each orthogonal linear polarization channel (Chuss et al. 2012b, 2014; Rostem et al. 2012; Appel et al. 2014). The bolometers are read out through time-division multiplexing (TDM) of superconducting quantum interference device (SQUID) amplifiers (Battistelli et al. 2008; Doriese et al. 2016). The CLASS Q-band two-stage TDM scheme consists of 8 columns multiplexing 11 rows of SQUIDs, for a total of 88 channels, of which 14 are dedicated dark SQUID channels used to characterize readout noise and magnetic field pickup. A dark SQUID is a readout channel that is not connected to a TES bolometer. Two readout channels are connected to dark TES bolometers fabricated within the polarimeter chips (Denis et al. 2009, 2016). Unlike the optical bolometers, the dark bolometers are not connected to antennas at the waveguide output of the feedhorns (Ade et al. 2009; Chuss et al. 2012b). Of the 72 polarization sensitive bolometers, 64 were operational during the first observing campaign; the remaining eight channels were lost during deployment due to a readout electronics failure. These channels were recovered for the second observing campaign, which began in 2018 June.

The Q-band telescope observed on a 24 hr cycle that started routinely at 14:00 UTC (late-morning local time). The Q-band receiver operates a dilution refrigerator that continuously cools the detector array to  $T_{\rm b} \approx 42\,{\rm mK}$  (Iuliano et al. 2018) during science operations, therefore allowing any observation cadence. Our 24 hr cycle is chosen to yield a full sky map each day at one boresight. We change boresight angle everyday, and the timing of the schedule end/start coincides with the site crew work schedule. At the beginning and end of an observation cycle, the detector bias voltage (V) was swept while recording the current response (I) to produce what will hereafter be called an "I-V curve." Additional I-V curves are acquired before special data sets such as wire-grid calibration measurements, and detector noise tests with the cryostat window covered. These I-V curves are used to choose the optimal bias voltage for each column composed of up to 10 TES bolometers. During observations these bias voltages place the array TES bolometers on their superconducting transition between 30% and 60% of their normal resistance. The detector saturation power  $(P_{sat})$  is extracted from I-V data and defined as the detector bias power (P = IV) evaluated at 80% of the TES normal resistance  $(R_N)$ . The difference between the  $P_{\text{sat}}$ measured in dark laboratory tests with the detectors enclosed in a 1 K cavity  $(P_{\odot})$ , and those measured while observing the sky is interpreted as the optical power loading  $(P_{\gamma})$  on the detectors. Included in this number is a correction for a small offset tracked by neighboring nonoptical bolometers  $(P_D)$  discussed in Section 2.1.

Detector responsivity ( $S = dI/dP_{\gamma}$ ) estimated from I-V data is used to calibrate current signals (dI) across the TES to power deposited on the bolometer  $(dP_{\gamma})$ . Detector optical time constants are extracted from the delayed response to the VPM synchronous signal (see Figure 2) that appears at the modulation frequency of 10 Hz. Combining measured time constants with I-V curve data, we derive the heat capacity of the bolometers. Table 1 summarizes median detector parameters across the array during this period.

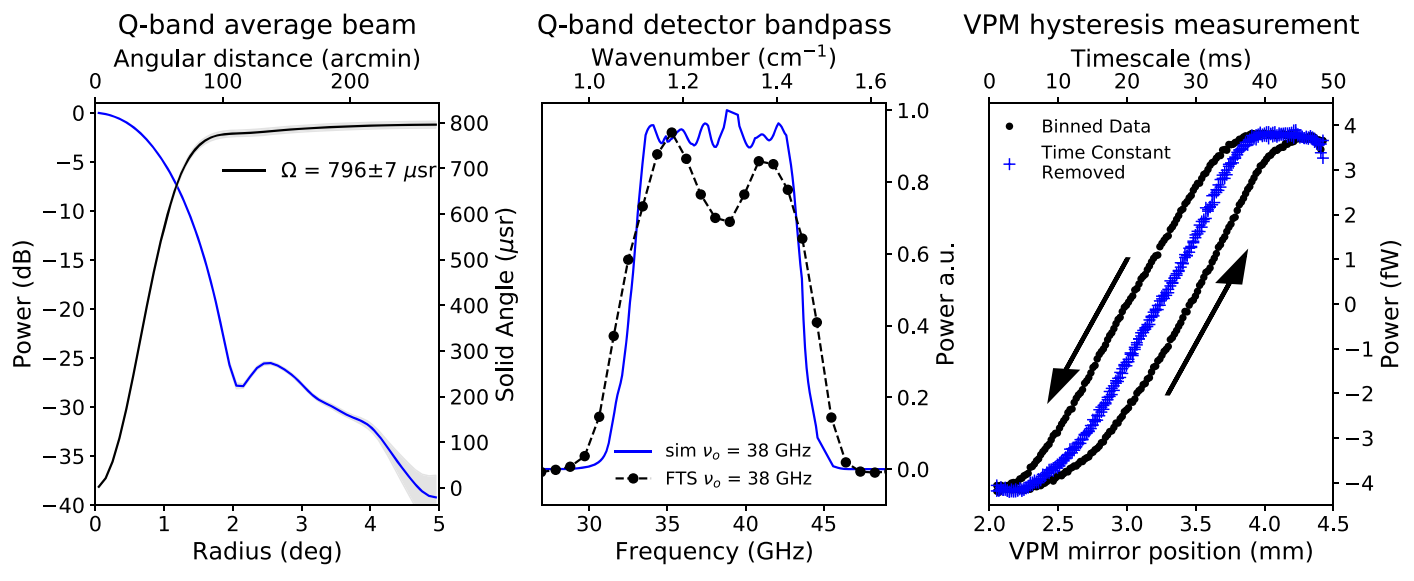


Figure 2. Left: the blue solid line shows the array-averaged radial beam profile derived from Moon observations, and the gray shaded region the measurement uncertainty. The main lobe is similar to a 1°5 Gaussian beam. The black line shows the array-averaged beam solid angle vs. radius with a total solid angle of 796  $\mu$ sr (Z. Xu et al. 2019, in preparation). Center: the solid line plots the simulated detector bandpass (Chuss et al. 2012b) with center frequency 38.0 GHz and bandwidth 11.4 GHz. The connected dots show a *Q*-band detector bandpass extracted from Fourier transform spectrometer (FTS) measurements made in the laboratory (see Dahal et al. 2018 for a description of the FTS testing setup). We use a Martin–Puplett FTS (T. Wei 2010, private communication; Martin & Puplett 1970) with a liquid nitrogen cooled blackbody (Petroff et al. 2019) as the input source while the FTS output is directed at a CLASS feedhorn-coupled *Q*-band bolometer placed one meter behind a 10 cm diameter cold stop. The feedhorn's frequency dependent gain (Zeng 2012) and the transmission of the lab-cryostat filters are divided out from the raw FTS measurement. The center frequency of the measured bandpass matches the simulation and has an estimated uncertainty of 0.2 GHz driven by the lab-cryostat filter transmission model. The  $\sim$ 1 GHz resolution of the FTS broadens the measured bandpass edges compared to the simulation. The remaining differences between the measured and simulated bandpass are likely due to unaccounted systematics of the FTS and/or the coupling optics. The detector bandpass corresponds to the effective telescope bandpass for a beam filling extended Rayleigh–Jeans (RJ) thermal source. The effective center frequency for a Rayleigh–Jeans point source is 38.5 GHz, obtained from combining the detector bandpass with the telescope frequency dependent gain (P. Fluxa 2019, in preparation). Right: the raw (black) and time-crostant corrected (blue) detector response to the VPM synchronous signal binned with respect to the gri

# 2.1. Optical Loading

The in-band (see bandpass in Figure 2) optical power  $P_{\gamma}$  dissipated on each bolometer is equal to the difference between the on-sky detector bias power P and the phonon power  $P_{\varphi}$  that flows from the bolometer island to the bath:

$$P_{\gamma} = P_{\varphi} - P,\tag{1}$$

where  $P_{\varphi}$  and the bias power P are both measured with the detector baseplate temperature at  $T_{\rm b}\approx 50\,{\rm mK}$  ( $P_{\varphi}$  is equivalent to  $P_{\rm sat}$  measured in dark laboratory tests with no optical loading). The detector copper baseplate serves as both mechanical support and thermal heatsink for the detector chips (Appel et al. 2014). Its temperature is tracked by a calibrated ruthenium oxide (ROX) temperature sensor. <sup>13</sup>

The Q-band array contains two dark TES bolometers that have similar electro-thermal properties to the optical detectors in the array, but are disconnected from the on-chip planar microwave circuitry that couples the radiation from a feedhorn to the optical TES bolometers in a pixel. The saturation power for these bolometers decreases on average by  $P_{\rm D}=0.5\,{\rm pW}$  when opening the 1 K detector cryostat volume to the sky. Daily changes in atmospheric conditions affect both P for optical detectors as well as  $P_{\rm D}$ . In particular, we find that averaged across the observing period  $P_{\rm D}/(P_{\varphi}-P)=0.26$ . The dark detector response to scanning an unresolved source like the Moon is <0.03% that of the average optical detector. Hence the change in dark detector saturation power can be interpreted as an offset in  $T_{\rm b}$  between the ROX and the silicon frame holding the bolometers, as opposed to optical

coupling. This offset can be driven by changes in the 1 K nylon filter (Essinger-Hileman et al. 2014; Iuliano et al. 2018) temperature ( $\sim$ 4 K at its center) as atmospheric conditions change, since radiation emitted by the filter would fill the focal plane volume and weakly couple to the detector chip and/or the ROX. We find less likely the alternative explanation of out-of-band power coupling directly to the TES island due to careful detector design isolating the TES bolometers from possible light leaks, and the lack of any out-of-band signal in our FTS measurements. We assume dark detector saturation power offset is similar for all bolometers in the array; hence, we subtract  $P_{\rm D}$  from  $P_{\gamma}$  for all optical channels.

The median in-band optical loading  $P_{\gamma}=1.6\,\mathrm{pW}$  is consistent with the model presented in Essinger-Hileman et al. (2014) and Appel et al. (2014). Two factors deviate from the model: (1) slightly lower optical efficiency in the field reduces  $P_{\gamma}$ , and (2) the instrument's baffle and mount enclosure structure source 0.2 pW of additional optical power.

# 2.2. Detector Responsivities and Time Constants

Of I–V derived detector responsivities across all CMB observations, 98% fall between 5 and 13  $\mu$ A pW $^{-1}$ . This well-defined range is due to stable atmospheric loading, stable cryogenic temperatures, and near-optimal detector saturation powers (Rostem et al. 2014a).

The VPM consists of a wire-grid that is placed in front of a mirror. The millimeter spacing between the mirror and the grid is optimized for the *Q*-band telescope (Harrington et al. 2018). In the CLASS telescopes, the mirror position is modulated at a frequency of 10 Hz to achieve polarization modulation. In addition to reflecting and modulating the polarized sky signal,

<sup>13</sup> RX-102A; https://www.lakeshore.com.

**Table 1**Table of *Q*-band Detector Parameters

TES Bolometer Parameters				
Phonon Power $(P_{\varphi})$	6.3 pW			
Bias Power (P)	4.2 pW			
Dark Power Offset $(P_D)$	0.5 pW			
Optical Loading $(P_{\gamma})$	1.6 pW			
Responsivity (S)	$-8.2~\mu\mathrm{A}~\mathrm{pW}^-$			
Optical Time Constant $(\tau_{\gamma})$	3.4 ms			
Thermal Time Constant $(\tau_{\varphi})$	17 ms			
Heat Capacity (C)	$3 \text{ pJ K}^{-1}$			
Thermal Conductivity ( <i>G</i> )	$177 \text{ pW K}^{-1}$			
Thermal Conductivity Constant $(\kappa)$	$13.4 \text{ nW K}^{-4}$			
Critical Temperature $(T_c)$	149 mK			
Normal Resistance $(R_N)$	$8.2~\mathrm{m}\Omega$			
Shunt Resistance $(R_{\rm sh})$	$0.25~\mathrm{m}\Omega$			
TES loop Inductance (L)	500 nH			

TES loop Inductance (L)	500 nH				
Optical Performance Parameters					
System Noise Temperature $(T_{sys})$	27 K				
Telescope Efficiency $(\eta)$	0.48				
RJ Temp Calibration $(\frac{dT_{RJ}}{dP_{\gamma}})$	$13.1 \text{ K pW}^{-1}$				
CMB-RJ Calibration $(\frac{dT_{\text{cmb}}}{dT_{\text{RJ}}})$	1.04				
Detector Dark Noise Power (NEP <sub>d</sub> )	11 aW√s				
Detector Total Noise Power (NEP)	$19 \text{ aW} \sqrt{\text{s}}$				
Detector Noise Temperature (NET)	$258  \mu \mathrm{K_{cmb}} \sqrt{\mathrm{s}}$				
Optical Detectors ( $N_{\text{det}}$ )	64				
Array Noise Temperature	$32  \mu K_{cmb} \sqrt{s}$				
RJ Extended Source Band Center ( $\nu_{\rm o}$ )	38.0 GHz				
RJ Point Source Band Center ( $\nu'_{o}$ )	38.5 GHz				
Bandwidth $(\Delta \nu)$	11.4 GHz				
Beam Solid Angle $(\Omega)$	796 $\mu$ sr				
RJ Point Source Flux Factor $(\Gamma)$	$27.6 \ \mu \text{K Jy}^{-1}$				

**Note.** Parameters on the left column are derived with the help of *I–V* data and represent the median value across the detector array. Time constant and heat capacity estimates also depend on measurements of the VPM synchronous signal. The right-hand side parameters are derived using: TOD power spectral density near the 10 Hz modulation frequency to estimate NEP, Moon observations to measure the beam solid angle and calibrate power at the bolometer to antenna temperature, and laboratory Fourier transform spectrometer (FTS) measurements to determine bandpass properties.

the VPM emits a small signal synchronous with the grid-mirror distance. Each subset of CMB TOD is fitted for a detector time constant that minimizes the hysteresis of this synchronous signal sourced by the VPM (see Figure 2). Eighty-six percent of CMB scans yield detector time constant  $(\tau_{\gamma})$  measurements between 2 and 6 ms. All are short enough to respond to the targeted 10 Hz modulation frequency and several of its harmonics. Multiplying  $\tau_{\gamma}$ by the electro-thermal feedback (Irwin & Hilton 2005) speed-up factor estimated from I-V data yields the detector thermal time constant  $(\tau_{\varphi})$ . The heat capacity (C) of each detector is then obtained by multiplying its average thermal time constant by the detector thermal conductivity (G). The measured average bolometer heat capacity is 3 pJ K<sup>-1</sup>. All detector heat capacities are within 1 pJ K<sup>-1</sup> of the mean. Achieving the targeted heat capacity allows for stable/optimal biasing of the detectors in the field, improving detector sensitivity and observing efficiency.

#### 2.3. Detector Noise

Detector noise performance is quantified in terms of noiseequivalent power (NEP) at the bolometer. We measure the NEP by averaging the PSD of the detector output in the side bands of the 10 Hz modulation frequency (9–11 Hz). To reduce correlated noise and improve the white noise estimate, we calculate individual detector NEP by first subtracting the TOD of detector pairs within a pixel (coupled to a feedhorn), then computing the PSD of the pair difference TOD and dividing by a factor of two in power squared units. Here we do not consider single detectors whose pair is not operational; hence, this NEP analysis focuses on 27 detector pairs.

The median single detector NEP in the first observing season is NEP =  $19\,\mathrm{aW}\sqrt{s}$ . This result is consistent with expectations once we correct the design estimates in Essinger-Hileman et al. (2014) to account for photon bunching noise cross-terms, lower achieved optical efficiency, and additional beam spill onto the baffle and telescope enclosure structure. Optical loading on the bolometers varies with atmospheric conditions; this allows us to probe the detector NEP versus  $P_{\gamma}$  relationship. Each  $I\!-\!V$  measurement yields a  $P_{\gamma}$  estimate for each detector, which corresponds to the NEP measured in the subsequent time-ordered data acquisition. We find that the change in  $P_{\gamma}$  and NEP between consecutive  $I\!-\!V$  measurements is small.

The NEP of a bolometer observing blackbody radiation is subject to both dark detector noise (NEP<sub>d</sub>) and photon noise (NEP $_{\gamma}$ ). For the CLASS TES bolometers, NEP<sub>d</sub> is dominated by phonon thermal fluctuations but also contains contributions from TES Johnson noise and SQUID readout noise. Tests in dark laboratory cryostats yield an average *Q*-band array NEP<sub>d</sub> =  $11 \, \text{aW} \sqrt{s}$  (Appel et al. 2014).

The statistical properties of the photons emitted by thermal sources we observe (atmosphere, CMB, dielectric filters, Moon, etc.) generate noise fluctuations at the detector output, which cannot be suppressed by improving the detector characteristics (van Vliet 1967; Mather 1982; Richards 1994; Zmuidzinas 2003). The average variance in the number of photons (n) per mode sourced by a blackbody at temperature T is  $\langle (\Delta n)^2 \rangle = \langle n \rangle + \langle n \rangle^2$ . The first term indicates that the blackbody photons obey Poisson statistics in the limit that  $n \ll 1$  ( $kT/h\nu \ll 1$ ), while in the limit  $n \gg 1$  ( $kT/h\nu \gg 1$ ), the second term dominates and the photons arrive in bunches. Here k is Boltzmann's constant and h is Planck's constant. Photon counting statistics are translated to NEP (NEP $_{\gamma}$ ) by identifying the spectral power density observed through a single mode detector as  $P_{\nu} = h\nu \langle n \rangle$ ; therefore (Richards 1994):

$$(\text{NEP}_{\gamma})^2 = \int h\nu P_{\nu} d\nu + \int P_{\nu}^2 d\nu \ (\text{W}^2 \text{ s}), \tag{2}$$

where  $\int P_{\nu}d\nu = P_{\gamma} \approx P_{\nu_0}\Delta\nu \approx \eta kT\Delta\nu$  (because the CMB and other sources CLASS *Q*-band observes are close to the Rayleigh–Jeans limit),  $\Delta\nu$  is the microwave signal bandwidth, and  $\eta$  is the optical efficiency of the entire telescope system, including attenuation, reflection, and beam spill due to the detector, filters, lenses, window, mirrors, VPM, and baffle.

The total detector NEP can be expressed in terms of measured quantities NEP<sub>d</sub>,  $P_{\gamma}$ ,  $\Delta\nu$ , and detector band center frequency  $\nu_{\rm o}$  as:

$$(\text{NEP})^2 = (\text{NEP}_d)^2 + h\nu_0 P_{\gamma} + \frac{P_{\gamma}^2}{\Delta \nu} (\text{W}^2 \text{s}).$$
 (3)

Figure 3 shows the measured NEP on the *y*-axis, and on the *x*-axis the corresponding measured  $P_{\gamma}$ . Equation (3) is fitted to the data points by setting  $\nu_{\rm o}=38.0\,{\rm GHz}$  and leaving NEP<sub>d</sub> and

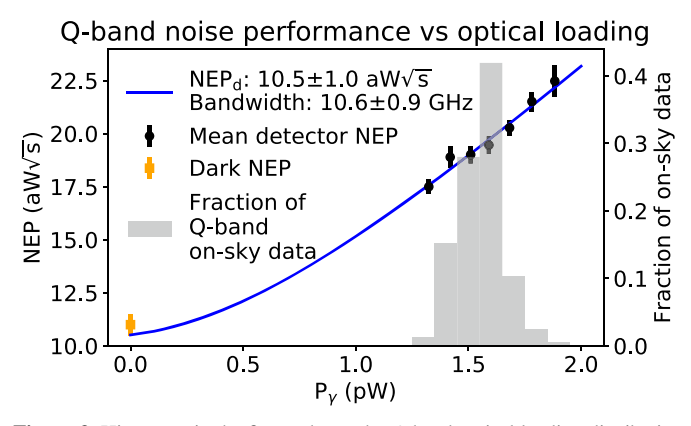


Figure 3. Histogram in the figure shows the *Q*-band optical loading distribution during observations. The relatively narrow range highlights the stability of the atmosphere at the CLASS site in the Atacama Desert of Chile. The black data points are the average NEP across the detector array for each bin of optical loading. The line is a model of on-sky NEP based on Equation (3) with the center frequency set to  $\nu_{\rm o}=38.0$  GHz, and the bandwidth  $\Delta\nu$  and dark detector NEP<sub>d</sub> left as free parameters to fit. The results of the fit are consistent with independent FTS and dark laboratory measurements of  $\Delta\nu$  and NEP<sub>d</sub> (see Table 1). The measured NEP<sub>d</sub> is plotted in orange at zero optical loading. *Q*-band NEP is dominated by bunching noise; therefore, sensitivity is driven by total optical loading and detector bandwidth. The model provides a quantitative prediction of instrument sensitivity as optical loading changes with the telescope design.

 $\Delta \nu$  as free parameters. The best-fit result of NEP<sub>d</sub> =10.5  $\pm$  1.0 aW  $\sqrt{s}$  and  $\Delta \nu$  = 10.6  $\pm$  0.9 GHz is consistent with independent measurements of 11 aW  $\sqrt{s}$  and 11.4 GHz. This confirms that the CLASS *Q*-band detectors are photon noise limited and that the NEP is dominated by the photon noise bunching term. This NEP model provides a quantitative understanding of possible sensitivity improvements to the instrument if optical loading can be reduced without decreasing optical efficiency. In particular, 300 K baffling configurations will be explored in future seasons, where control of systematic effects due to beam spill can be traded for sensitivity.

# 3. Moon Observations and Calibration to Antenna Temperature

The electrical current signal from each TES detector is calibrated to power deposited on its bolometer island through responsivity estimates from the most recent I-V acquisition. For the entire array, we find one calibration factor  $(dT_{\rm RJ}/dP_{\gamma})$  from power deposited at the bolometer  $(dP_{\gamma})$  to antenna (Rayleigh–Jeans) temperature  $(dT_{\rm RJ})$  on the sky. At 38.0 GHz, the conversion factor from  $dT_{\rm RJ}$  to CMB thermodynamic temperature  $(dT_{\rm cmb})$  is  $dT_{\rm cmb}/dT_{\rm RJ}=1.04$ . Individual detector TODs are calibrated to the array standard (i.e., the average) through a relative calibration factor  $\epsilon_j$  equivalent to the inverse relative optical efficiency of the detector. Hence a small  $dI_j$  signal of detector j is calibrated to  $dT_{\rm cmb}$  units through

$$dT_{\rm cmb} = \epsilon_j \frac{dT_{\rm cmb}}{dT_{\rm RJ}} \frac{dT_{\rm RJ}}{dP_{\gamma}} \frac{dI_j}{S_j^k},\tag{4}$$

where k identifies the I-V used to estimate the detector responsivity  $S_j^k$ .

The Moon is an excellent target to constrain the absolute and relative calibrations of the CLASS *Q*-band detectors. At radio and millimeter wavelengths, the Moon radiates like a graybody, with frequency dependent brightness temperature established

by the optical depth of the lunar regolith and its thermal properties (Linsky 1966; Troitskii 1967). Unlike visible light, the scattering of microwave radiation from the Sun off the Moon's surface is negligible compared to its thermal emission.

The Moon's angular size of half a degree and  $\sim 200 \, \mathrm{K}$  temperature at Q band approximates a point source for the 1°.5 CLASS beam. When aligned with the beam center, the array-averaged peak Moon power measured at the bolometers is  $P_{\mathrm{m}} \sim 1.3 \, \mathrm{pW}$ , which is one-third of the average detector saturation power. The TES response is linear throughout the full range of the Moon signal, and a signal-to-noise ratio of  $\sim 100,000$  is achieved. This allows the measurement of detector pointing, beams, and calibration factors from the nominal 720° azimuth scan data whenever the Moon is in the field of view, increasing the observing efficiency by reducing time spent conducting targeted scans.

The absolute and relative detector calibrations extracted from Moon observations depend on the size of the average detector beam (see Figure 2) and the angular extent and brightness temperature of the Moon ( $T_{\rm m}$ ) at 38.5 GHz on the date of observation. Moon-centered maps indicate the average detector beam matches the full width at half maximum (FWHM) design target of 1°.5 (see Figure 2). The average Moon angular diameter ( $D_{\rm m}$ ) of 31 arcminutes corresponds to a beam power dilution factor ( $\eta_{\rm m}$ ) given by the ratio of the moon solid angle ( $\Omega_{\rm m}$ ) to the solid angle of the convolution of the beam with the moon ( $\Omega'$ ),  $\eta_{\rm m} = \Omega_m/\Omega' = 0.077$ . This dilution factor makes the peak Moon antenna temperature  $T_{\rm m}^A = \eta_{\rm m} T_{\rm m} \sim 16~{\rm K}$ . Tidal locking of the Moon's rotation and its orbit results in

one hemisphere of the Moon always facing the Earth. The Moon's brightness temperature averaged across its Earth-facing hemisphere and across the lunar cycle  $(\overline{T}_m)$  has been accurately measured at Q band with the aid of an "artificial Moon" calibrator (Krotikov & Troitskiĭ 1964; Troitsky et al. 1968; Troitskii & Tikhonova 1970; Krotikov & Pelyushenko 1987). At 35 GHz, Krotikov & Pelyushenko (1987) reports  $\overline{T}_{\rm m}=211\pm5~{\rm K}$ , and at 44 GHz,  $\overline{T}_{\rm m}=208\pm5~{\rm K}$ . For the CLASS 38.5 GHz center frequency, we take  $\overline{T}_{\rm m}=210\pm5~{\rm K}$ . Linsky (1973) proposed using the brightness temperature at the center of the lunar disk as a radiometric standard for wavelengths between 10  $\mu$ m and 1 m. Near 8 mm wavelengths, Linsky (1973) estimates a time-averaged brightness temperature at the center of the lunar disk of  $\sim$ 230 K. Note that the brightness temperature averaged across the entire lunar disk is lower than at the center due to colder temperatures near the poles. More recently, the ChangE satellite (Zheng et al. 2012) mapped the Moon temperature at 37 GHz with high resolution; unfortunately, the absolute calibration is less reliable due to beam side-lobe pickup of the cold antenna reference (Tsang et al. 2016; Hu et al. 2017).

The temperature of the Moon's Earth-facing hemisphere oscillates with the fraction of Sun illumination or Moon phase (see bottom panel of Figure 4). At Q band, the maximum  $T_{\rm m}$  peaks a few days after full Moon due to the heat capacity and thermal conductivity of the Moon's surface material (Troitskii 1967). The Moon phase follows on average a 29.53 day cycle, while the Moon orbital period is 27.32 days. The Moon's elliptical orbit around Earth (strongly perturbed by the Sun) changes its angular diameter  $D_{\rm m}$  on the sky, as shown in the middle panel of Figure 4. The two distinct periods of the Moon's temperature and angular diameter oscillations cause a beat pattern in the measured antenna temperature  $(T_{\rm m}^A)$ , see the top panel

 $<sup>\</sup>overline{d^{14}} dT_{\text{cmb}}/dT_{\text{RJ}} \approx (e^{x_0} - 1)^2/x_0^2 e^{x_0} \text{ where } x_0 = h \nu_0/kT_{\text{cmb}}.$ 

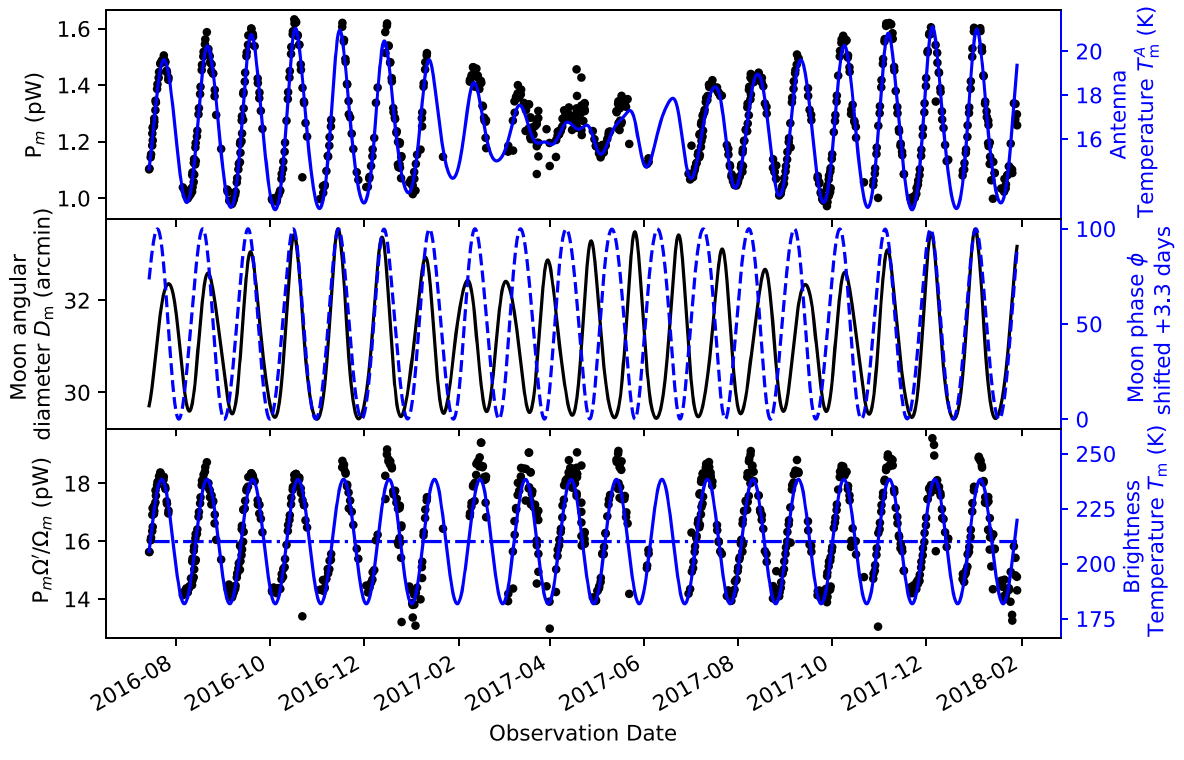


Figure 4. Top: data points are the array-averaged peak Moon power measured at the bolometers ( $P_{\rm m}$ ) across the observing period. The solid line is a model of the Moon's antenna temperature based on the CLASS Q-band beam solid angle, the Moon's time-dependent angular diameter, the Moon's temperature oscillations that follow its phase, and an absolute calibration to a mean Moon temperature of 210 K at 38.5 GHz (Krotikov & Pelyushenko 1987). Middle: the solid line plots the Moon's angular diameter over time. The 27 day elliptical Moon orbit around the Earth is perturbed by the Sun. The dashed line plots the Moon phase delayed by 3.3 days to compensate for the measured lag in Moon brightness temperature. The 27 day orbital period and 29.5 day phase period interact to create the beat pattern observed in the top panel. Bottom: data points from the top panel are divided by the beam-Moon dilution factor ( $\eta_{\rm m} = \Omega_{\rm m}/\Omega'$ ). The solid line plots the Moon's brightness temperature model described by Equation (5), with its parameters calibrated to match a mean temperature of 210 K marked with the dashed line. Differences between the data points and the model may be the result of weather, instrumental systematics, and/or limitations of the Moon emission model. Future work will explore implementing additional data quality tools and introducing a more complex Moon thermal model.

Table 2
Table of Tau A Flux Measurements between 30 and 44 GHz

Instrument	Year	$\nu_e$ (GHz)	Flux (Jy)	Flux 2017 (Jy)	Flux 2017 at 38.4 GHz (Jy)	References
NRL	1966	31.4	$387 \pm 87$	$344 \pm 77$	321 ± 73	Hobbs et al. (1968)
AFCRL	1967	34.9	$340^{+65}_{-40}$	$303^{+58}_{-36}$	$293^{+57}_{-36}$	Kalaghan & Wulfsberg (1967)
CBI	2000	31	$355.3 \pm 18$	$341.7 \pm 17$	$317 \pm 19$	Cartwright et al. (2005); Cartwright (2003)
VSA	2001	33	$322 \pm 4$	$310 \pm 4$	$294 \pm 11$	Hafez et al. (2008)
WMAP	2005	32.96	$342.8 \pm 6.4$	$333.5 \pm 6.2$	$316 \pm 12$	Weiland et al. (2011)
WMAP	2005	40.64	$317.7 \pm 8.6$	$307.9 \pm 8.4$	$314 \pm 13$	Weiland et al. (2011)
Planck	2011	30	$344.23 \pm 0.27$	$339.51 \pm 0.34$	$311 \pm 10$	Planck Collaboration et al. (2016c)
Planck	2011	44	$292.68 \pm 0.23$	$288.14 \pm 0.41$	$302 \pm 10$	Planck Collaboration et al. (2016c)
CLASS	2017	38.4	$308\pm11$	$308 \pm 11$	$308\pm11$	This paper

Note. The reported Tau A flux measurements are referenced to Epoch 2017 by applying a per-year flux variation of  $-0.23 \pm 0.01\%$  yr<sup>-1</sup> for measurements between 30 GHz and 36 GHz and  $-0.26 \pm 0.02\%$  yr<sup>-1</sup> for measurements between 38 GHz and 44 GHz (Weiland et al. 2011). The uncertainty on the yearly flux variation is propagated to the 2017 flux errors. The measurements are converted to 2017 Flux at 38.4 GHz by applying the *WMAP* spectral model with a power index of  $-0.350 \pm 0.026$  and propagating the model uncertainty. In the 1960s, Tau A was observed with the 8.8 m microwave antenna at the Air Force Cambridge Laboratories (AFCRL) and with the 25.9 m paraboloidal reflector at the Naval Research Laboratory's (NRL) Maryland Point Observatory. In the early 2000s, it was observed by the Very Small Array (VSA) located at the Teide Observatory, Izaña, Tenerife and by the Cosmic Background Imager (CBI) from the Llano de Chajnantor in Northern Chile. Measurements by the *Wilkinson Microwave Anisotropy Probe* (*WMAP*) satellite between 2002 and 2008 are referenced to 2005, while the *Planck* satellite's 2009 to 2013 observations are referenced to 2011.

of Figure 4). For example, in 2017 May the peak  $T_{\rm m}$  coincided with minimum  $D_{\rm m}$ , nulling the fluctuation in  $T_{\rm m}^A$ , while the opposite effect occurred in 2016 November and 2017 December.

To isolate the  $T_{\rm m}$  oscillation from the Moon angular size variations, the  $P_{\rm m}$  measurements across the observing era are divided by the time-dependent beam-Moon dilution factor  $\eta_{\rm m}$ :

 $P_{\rm m}'=P_{\rm m}/\eta_{\rm m}.$   $P_{\rm m}'$  data points are fit to a simple sinusoidal model over time t:

$$P'_{\rm m} = P'_0 + P'_1 \cos(2\pi t/t_0 + \phi), \tag{5}$$

where  $P_0'$  is the average brightness,  $P_1'$  is the amplitude of the brightness fluctuations,  $t_0$  the period of the oscillation, and  $\phi$ 

the offset from full Moon. As expected, the fit yields  $t_0 = 29.5$  days, the same as the Moon phase period, and  $\phi = 3.3$  days after full Moon, indicating a lag between full Moon illumination and maximum brightness temperature.  $P'_0$  equals 16.0 pW, and  $P'_1$  equals 2.2 pW (see the bottom panel of Figure 4).

The Moon disk blocks the CMB radiation behind it; therefore,  $P_{\rm m}'$  measures the difference between  $T_{\rm m}$  and the background CMB brightness temperature at 38.0 GHz,  $T_{\rm cmb}^B=1.9~{\rm K}$ .  $T_{\rm cmb}^B$  is less than the CMB's blackbody temperature  $T_{\rm cmb}=2.725~{\rm K}$  (Fixsen 2009) due to the brightness temperature definition, which is based on the Rayleigh–Jeans approximation. The CMB temperature was not known when the "artificial moon" observations were made; therefore, we interpret their reported average Moon temperature to be measured with respect to the CMB background:  $\overline{T}_{\rm m}=\langle T_{\rm m}-T_{\rm cmb}^B\rangle$ . Note that the background CMB brightness temperature is less than 1% (and well within the uncertainty) of  $\overline{T}_{\rm m}$ .

The array's absolute calibration factor is given by the ratio of the reported average Moon brightness temperature  $\overline{T}_{\rm m}$  and the array-averaged brightness power  $P_0'$ :

$$\frac{dT_{\rm RJ}}{dP_{\gamma}} = \frac{\overline{T}_{\rm m}}{P_0'} = 13.1 \pm 0.3 \,\,{\rm K \, pW^{-1}}, \,\,{\rm and}$$
 (6)

$$\frac{dT_{\rm cmb}}{dP_{\gamma}} = \frac{\overline{T}_{\rm m}}{P_0'} \frac{dT_{\rm cmb}}{dT_{\rm RJ}} = 13.6 \pm 0.3 \text{ K pW}^{-1}.$$
 (7)

This absolute calibration factor translates to a telescope optical efficiency of:

$$\eta = \left(k\Delta\nu \frac{dT_{\rm RJ}}{dP_{\gamma}}\right)^{-1} = 0.48 \pm 0.02,$$
(8)

where the uncertainty on  $\eta$  is driven by the uncertainty on  $\Delta\nu$  ( $\sigma_{\Delta\nu}=0.5\,\mathrm{GHz}$ ).

Relative calibration factors  $\epsilon_j$  between detectors are obtained by dividing the array average Moon amplitude by the individual bolometer Moon measurement. These relative factors account for small differences in beam solid angle, bandpass, and optical efficiency across the detector array. Moon data indicate that these are constant throughout the observing period and fall between 0.9 and 1.1.

The NEP noise measurements are multiplied by  $dT_{\rm cmb}/dP_{\gamma}$  to obtain median single detector NET = 258  $\mu \rm K_{\rm cmb} \sqrt{s}$ . The average  $P_{\gamma} = 1.6 \, \rm pW$  is equivalent to an antenna temperature of  $T_{\gamma} = P_{\gamma}/(\eta k \Delta \nu) = 21 \, \rm K$ . We estimate that 5 K is from emission or spill within the cryostat (Iuliano et al. 2018; 1 K, 4 K, and 60 K filters and lenses; 4 K cold stop; and 300 K filters and window), 6 K originates from the rest of the telescope (mirrors, VPM, closeout, mount enclosure, and baffle), 8 K comes from atmospheric emission, and 1.9 K from the CMB. The system noise temperature,  $T_{\rm sys} = {\rm NEP}/\eta k \sqrt{\Delta \nu} = 27 \, {\rm K}$ , implies an effective detector noise temperature of  $T_{\rm det} = T_{\rm sys} - T_{\gamma} = 6 \, {\rm K}$ .

## 4. Tau A Intensity at O Band

The Crab Nebula, or Tau A, is the remnant of supernova SN 1054. Its spectral energy density from radio to millimeter wavelengths follows a power-law emission model with spectral index  $\beta = -0.323$  (Ritacco et al. 2018). Flux density measurements of Tau A between 30 and 44 GHz are compiled

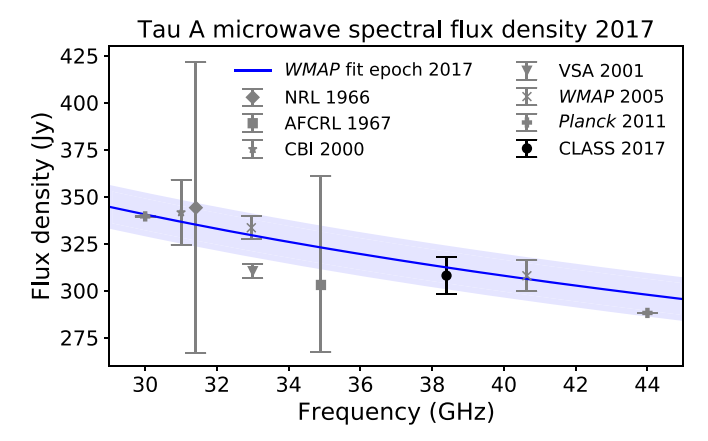


**Figure 5.** Tau A flux density measurements found in Table 2 and referenced to epoch 2017. The solid line is the *WMAP* 22 to 93 GHz Tau A flux density vs. frequency model:  $\log S({\rm Jy}) = 2.502-0.350 \, \log(\nu/40 \, {\rm GHz})$  (Weiland et al. 2011), referenced to epoch 2017. The shaded region is the  $1\sigma$  contour of the model's flux prediction including spectral and time evolution uncertainty. The CLASS intensity map calibrated through the Moon yields a Tau A flux density of  $308 \pm 11 \, {\rm Jy}$  at  $\nu_e = 38.4 \pm 0.2 \, {\rm GHz}$ . The  $796 \, \mu {\rm sr}$  CLASS beam solid angle dilutes Tau A to an antenna temperature of  $8.56 \pm 0.27 \, {\rm mK}$ .

in Table 2. Multiyear measurements from the *Wilkinson Microwave Anisotropy Probe (WMAP)* establish a precise model for the time and frequency dependent intensity of Tau A between 22 and 93 GHz (Weiland et al. 2011). This model predicts a Tau A flux density of 312 Jy at 38.4 GHz referenced to epoch 2017.

We extract a  $6 \times 6$  square-degree intensity map centered at Tau A from preliminary per-detector constant elevation scan (CES) maps covering 75% of the sky. These maps contain 72 CES that are 10 to 23 hr long. We generate simulated maps based on the *WMAP Q*-band intensity map, that incorporate the CLASS beam, scan strategy, and TOD filtering. The simulations indicate that the peak Tau A amplitude is reduced by 5%–6% in the preliminary CLASS maps due to the high-pass filter applied to the TODs. This bias is corrected, and the results from the 41 detectors that point low enough on the sky to observe Tau A are averaged.

Tau A's  $7 \times 5$  arcmin<sup>2</sup> (Green 2009) or 3  $\mu$ sr angular extent makes it effectively a point source when compared to the Q-band beam solid angle ( $\Omega = 796 \pm 7 \,\mu$ sr). The CLASS map of Tau A is consistent with the CLASS beam derived from moon measurements (FWHM  $\approx 1^{\circ}.5$ , see Figure 2) with a peak amplitude of  $T_A = 8.56 \pm 0.27 \,\mathrm{mK}$ . For the CLASS Q-band instrument, the peak amplitude in antenna temperature (K) is converted to spectral flux density (Jy) for an unresolved (i.e., point) source through the factor (Page et al. 2003a; Jarosik et al. 2011)

$$\Gamma = \frac{c^2}{2k\Omega\nu_e^2} = 27.8 \pm 0.5 \,\mu\text{K Jy}^{-1},$$
 (9)

where the effective central frequency of Tau A across the CLASS Q bandpass is  $\nu_e = 38.4 \pm 0.2 \, \mathrm{GHz}.^{15}$ 

Dividing the peak temperature measured for Tau A by  $\Gamma$  gives a flux density of 308  $\pm$  11 Jy. Figure 5 plots the flux density measurements tabulated in Table 2. The *WMAP* Tau A

<sup>15</sup> Effective frequency for a point source is defined as  $\nu_e = \int \nu \nu^{\alpha} f(\nu) d\nu / \int \nu^{\alpha} f(\nu) d\nu$ , where  $f(\nu)$  describes the instrument response (passband etc.),  $\alpha$  parametrizes the point-source flux density  $S = S_e(\nu/\nu_e)^{-\alpha}$ , and  $\alpha = -0.3$  for Tau A (Page et al. 2003b).

flux density model, which includes a yearly rate of decline and a spectral index, matches well with the measurements in the 30 and 44 GHz frequency range. Note that the reported CLASS Tau A flux density is independent of CMB calibration and rather is anchored to the Moon brightness temperature. In other words, the Tau A measurement shows that the CLASS antenna temperature calibration based on Moon observations is consistent with the *WMAP* calibration based on the CMB dipole.

#### 5. Conclusion

In this paper, we have established the basic on-sky performance of the CLASS telescopes. The stability and time constants of the Q-band TES bolometers are within specification. The array average 1.6 pW optical loading,  $19 \text{ aW} \sqrt{s} \text{ NEP}$ , and 27 K system noise temperature satisfy the design targets. A  $13.1 \pm 0.3 \,\mathrm{K} \,\mathrm{pW}^{-1}$  calibration factor that converts from optical power measured at the bolometer to Rayleigh-Jeans temperature on the sky is obtained from fitting hundreds of Moon observations to a Moon brightness temperature model that follows the Moon's orbit and phase. This calibration factor translates to a telescope optical efficiency of  $0.48 \pm 0.02$  and is used to construct a Tau A intensity map from the nominal CMB scans. We report a Tau A flux density of 308  $\pm$  11 Jy at  $38.4 \pm 0.2 \, \mathrm{GHz}$ , consistent with the WMAP Tau A timedependent spectral flux density model. The  $1\sigma$  error of the CLASS measurement includes the uncertainty in the bandpass center frequency, the calibration to antenna temperature, and the Tau A peak amplitude.

Between 2016 June and 2018 March, CLASS carried out the largest ground-based Q-band CMB sky survey to date, covering 75% of the sky. Comparable large-scale ground-based surveys at low-frequencies include Génova-Santos et al. (2017) and Jones et al. (2018). During this initial CLASS observing campaign, 64 Q-band bolometers were optically sensitive, with a median per-detector NET of 258  $\mu K_{cmb} \sqrt{s}$ , which implies a median instantaneous array sensitivity of 32  $\mu K_{cmb} \sqrt{s}$ . For comparison, the combined polarization sensitivity of the four WMAP 41 GHz radiometers was 469  $\mu K_{cmb} \sqrt{s}$  (Jarosik et al. 2003), and the combined sensitivity of the six Planck 44 GHz radiometers was 174  $\mu K_{cmb} \sqrt{s}$  (Planck Collaboration et al. 2016a).

This is the first of a series of papers to be published on the initial two years of CLASS 40 GHz observations. Additional articles will present the CLASS beam and window function, CLASS polarization modulation and stability, CMB survey maps, and science results derived therefrom. Beyond the first two years, the 40 GHz telescope continues to acquire data together with a 90 GHz telescope that was installed in 2018. An additional telescope at 90 GHz and a 150/220 dichroic telescope will be installed in the near future. The nominal survey ends in late 2021 with plans for extensions thereon.

We acknowledge the National Science Foundation Division of Astronomical Sciences for their support of CLASS under Grant Numbers 0959349, 1429236, 1636634, and 1654494. The CLASS project employs detector technology developed under several previous and ongoing NASA grants. Detector development work at JHU was funded by NASA grant number NNX14AB76A. K.H. is supported by NASA Space Technology Research Fellowship grant number NX14AM49H. B.P. is supported by the Fondecyt Regular Project No. 1171811

(CONICYT) and CONICYT-PFCHA Magister Nacional Scholarship 2016-22161360. We thank the anonymous reviewer for the careful reading of our manuscript and the many insightful comments and suggestions. We thank Philip Mauskopf for useful discussions on bolometer noise. We acknowledge important contributions from Keisuke Osumi, Mark Halpern, Mandana Amiri, Gary Rhodes, Janet Weiland, Mario Aguilar, Yunyang Li, Isu Ravi, Tiffany Wei, Connor Henley, Max Abitbol, Lindsay Lowry, and Fletcher Boone. We thank William Deysher, Maria Jose Amaral, and Chantal Boisvert for administrative support. We acknowledge productive collaboration with Dean Carpenter and the JHU Physical Sciences Machine Shop team. Part of this research project was conducted using computational resources at the Maryland Advanced Research Computing Center (MARCC). Some of the results in this paper have been derived using the HEALPix package (Górski et al. 2005). We further acknowledge the very generous support of Jim and Heather Murren (JHU A&S '88), Matthew Polk (JHU A&S Physics BS '71), David Nicholson, and Michael Bloomberg (JHU Engineering '64). CLASS is located in the Parque Astronómico Atacama in northern Chile under the auspices of the Comisión Nacional de Investigación Científica y Tecnológica de Chile (CONICYT). R.D. and P.F. thank CONICYT for grants Anillo ACT-1417, QUIMAL 160009, and BASAL AFB-170002.

#### **ORCID iDs**

John W. Appel <sup>®</sup> https://orcid.org/0000-0002-8412-630X Zhilei Xu (徐智磊) <sup>®</sup> https://orcid.org/0000-0001-5112-2567 Kathleen Harrington <sup>®</sup> https://orcid.org/0000-0003-1248-9563

Duncan J. Watts https://orcid.org/0000-0002-5437-6121 Edward J. Wollack https://orcid.org/0000-0002-7567-4451 Lingzhen Zeng https://orcid.org/0000-0001-6924-9072

#### References

Ade, P. A. R., Chuss, D. T., Hanany, S., et al. 2009, JPhCS, 155, 012006 Albrecht, A., & Steinhardt, P. J. 1982, PhRvL, 48, 1220 Allison, R., Caucal, P., Calabrese, E., Dunkley, J., & Louis, T. 2015, PhRvD, 92, 123535

Appel, J. W., Ali, A., Amiri, M., et al. 2014, Proc. SPIE, 9153, 91531J
Battistelli, E. S., Amiri, M., Burger, B., et al. 2008, JLTP, 151, 908
Bennett, C. L., Larson, D., Weiland, J. L., et al. 2013, ApJS, 208, 20
BICEP2 Collaboration, Keck Array Collaboration, Ade, P. A. R., et al. 2016, PhRvL, 116, 031302

BICEP2 Collaboration, Keck Array Collaboration, Ade, P. A. R., et al. 2018, PhRvL, 121, 221301

Bustos, R., Rubio, M., Otárola, A., & Nagar, N. 2014, PASP, 126, 1126 Cartwright, J. K. 2003, PhD thesis, Caltech

Cartwright, J. K., Pearson, T. J., Readhead, A. C. S., et al. 2005, ApJ, 623, 11 Chuss, D. T., Ali, A., Appel, J. W., et al. 2014, AAS Meeting, 223, 439.03

```
Chuss, D. T., Bennett, C. L., Costen, N., et al. 2012b, JLTP, 167, 923
Chuss, D. T., Wollack, E. J., Henry, R., et al. 2012a, ApOpt, 51, 197
Dahal, S., Ali, A., Appel, J. W., et al. 2018, Proc. SPIE, 10708, 107081Y
Denis, K. L., Ali, A., Appel, J., et al. 2016, JLTP, 184, 668
Denis, K. L., Cao, N. T., Chuss, D. T., et al. 2009, in AIP Conf. Ser. 1185, The
   Thirteenth International Workshop on Low Temperature Detectors-LTD13,
   ed. B. Young, B. Cabrera, & A. Miller (Melville, NY: AIP), 371
Doriese, W. B., Morgan, K. M., Bennett, D. A., et al. 2016, JLTP, 184, 389
Eimer, J. R., Bennett, C. L., Chuss, D. T., et al. 2012, Proc. SPIE, 845220
Essinger-Hileman, T., Ali, A., Amiri, M., et al. 2014, Proc. SPIE, 915311
Fixsen, D. J. 2009, ApJ, 707, 916
Génova-Santos, R., Rubiño-Martín, J. A., Peláez-Santos, A., et al. 2017,
          S, 464, 4107
Górski, K. M., Hivon, E., Banday, A. J., et al. 2005, ApJ, 622, 759
Green, D. A. 2009, BASI, 37, 45
Guth, A. H. 1981, PhRvD, 23, 347
Hafez, Y. A., Davies, R. D., Davis, R. J., et al. 2008, MNRAS, 388, 1775
Harrington, K., Eimer, J., Chuss, D. T., et al. 2018, Proc. SPIE, 10708, 107082M
Harrington, K., Marriage, T., Ali, A., et al. 2016, Proc. SPIE, 9914, 99141K
Henning, J. W., Sayre, J. T., Reichardt, C. L., et al. 2018, ApJ, 852, 97
Hinshaw, G., Larson, D., Komatsu, E., et al. 2013, ApJS, 208, 19
Hobbs, R. W., Corbett, H. H., & Santini, N. J. 1968, ApJ, 152, 43
Hu, G.-P., Chan, K. L., Zheng, Y.-C., Tsang, K. T., & Xu, A.-A. 2017, Icar,
  294, 72
Irwin, K., & Hilton, G. 2005, in Cryogenic Particle Detection, ed. C. Enss
   (Berlin: Springer), 81
Iuliano, J., Eimer, J., Parker, L., et al. 2018, Proc. SPIE, 10708, 1070828
Jarosik, N., Barnes, C., Bennett, C. L., et al. 2003, ApJS, 148, 29
Jarosik, N., Bennett, C. L., Dunkley, J., et al. 2011, ApJS, 192, 14
Jones, M. E., Taylor, A. C., Aich, M., et al. 2018, MNRAS, 480, 3224
Kalaghan, P. M., & Wulfsberg, K. N. 1967, AJ, 72, 1051
Kamionkowski, M., Kosowsky, A., & Stebbins, A. 1997, PhRvD, 55, 7368
Kovac, J. M., Leitch, E. M., Pryke, C., et al. 2002, Natur, 420, 772
Krotikov, V. D., & Pelyushenko, S. A. 1987, SvA, 31, 216
Krotikov, V. D., & Troitskiĭ, V. S. 1964, SvPhU, 6, 841
Kusaka, A., Appel, J., Essinger-Hileman, T., et al. 2018, JCAP, 9, 005
Kusaka, A., Essinger-Hileman, T., Appel, J. W., et al. 2014, RScI, 85, 024501
Linde, A. D. 1982, PhLB, 108, 389
Linsky, J. L. 1966, Icar, 5, 606
Linsky, J. L. 1973, ApJS, 25, 163
Louis, T., Grace, E., Hasselfield, M., et al. 2017, JCAP, 6, 031
```

```
Martin, D. H., & Puplett, E. 1970, InfPh, 10, 105
Mather, J. C. 1982, ApOpt, 21, 1125
Miller, N. J., Chuss, D. T., Marriage, T. A., et al. 2016, ApJ, 818, 151
Page, L., Barnes, C., Hinshaw, G., et al. 2003a, ApJS, 148, 39
Page, L., Jackson, C., Barnes, C., et al. 2003b, ApJ, 585, 566
Petroff, M., Appel, J., Rostem, K., et al. 2019, RScI, 90, 024701
Planck Collaboration, Ade, P. A. R., Aghanim, N., et al. 2015, A&A,
  576, A104
Planck Collaboration, Ade, P. A. R., & Aghanim, N. 2016a, A&A, 594, A2
Planck Collaboration, Ade, P. A. R., & Aghanim, N. 2016b, A&A, 594, A20
Planck Collaboration, Ade, P. A. R., & Aghanim, N. 2016c, A&A, 594, A26
Planck Collaboration, Aghanim, N., Akrami, Y., et al. 2018a, arXiv:1807.
Planck Collaboration, Akrami, Y., Arroja, F., et al. 2018b, arXiv:1807.06211
Planck Collaboration, Akrami, Y., Ashdown, M., et al. 2018c, arXiv:1807.
  06208
Planck Collaboration, Akrami, Y., Ashdown, M., et al. 2018d, arXiv:1801.
  04945
Planck Collaboration Int. L. 2017, A&A, 599, A51
Polarbear Collaboration, Ade, P. A. R., Akiba, Y., et al. 2014, ApJ, 794, 171
Rees, M. J. 1968, ApJL, 153, L1
Richards, P. L. 1994, JAP, 76, 1
Ritacco, A., Macías-Pérez, J. F., Ponthieu, N., et al. 2018, A&A, 616, A35
Rostem, K., Ali, A., Appel, J. W., et al. 2014b, Proc. SPIE, 9153, 91530B
Rostem, K., Bennett, C. L., Chuss, D. T., et al. 2012, Proc. SPIE, 84521N
Rostem, K., Chuss, D. T., Colazo, F. A., et al. 2014a, JAP, 115, 124508
Sato, K. 1981, MNRAS, 195, 467
Starobinsky, A. A. 1982, PhLB, 117, 175
Troitskii, V. S. 1967, R&QE, 10, 709
Troitskii, V. S., & Tikhonova, T. V. 1970, R&QE, 13, 981
Troitsky, V. S., Burov, A. B., & Alyoshina, T. N. 1968, Icar, 8, 423
Tsang, K., Hu, G.-P., & Zheng, Y.-C. 2016, AAS/DPS Meeting, 48,
  223.06
van Vliet, K. M. 1967, ApOpt, 6, 1145
Watts, D. J., Larson, D., Marriage, T. A., et al. 2015, ApJ, 814, 103
Watts, D. J., Wang, B., Ali, A., et al. 2018, ApJ, 863, 121
Weiland, J. L., Odegard, N., Hill, R. S., et al. 2011, ApJS, 192, 19
Zaldarriaga, M., & Seljak, U. 1997, PhRvD, 55, 1830
Zeng, L. 2012, PhD thesis, The Johns Hopkins Univ.
Zheng, Y. C., Tsang, K. T., Chan, K. L., et al. 2012, Icar, 219, 194
Zmuidzinas, J. 2003, ApOpt, 42, 4989
```